Wiley Analytical Science

The Current State of Reconstruction Technologies for 3D X-ray Microscopy including Algorithmic Innovation for AI-based Recovery

April 26, 10:00am - 11:00am EDT

Many properties can only be fully understood in 3D, such as porosity and tortuosity in porous materials, network connection maps in neuroscience, or mechanical properties in 3D additively manufactured structures. X-ray microscopy provides a unique method to image samples non-destructively in 3D across a wide range of materials and life sciences.

Watch this session during the WAS Virtual Conference:

Nicolas Guenichault, Ph.D.   **Dr. Stephen T. Kelly, Ph.D.**

Register Now

This talk is sponsored by **ZEISS**

Biodiversity Benefits for Size Modulation of Metal Nanoparticles to Achieve In Situ Semi-Oxidation toward Optimized Electrocatalytic Oxygen Evolution

Jia Zhang, Rong-Zhi Sun, Xue-Feng Zhang, Jun-Xi Wu, Yu-Hai Dou, Xuan-Yi Zhu, Li-Hong Yu, Lu-Yao Guo, Min-Ling Liu, Lin Guo, Li-Ming Cao, Chun-Ting He,* and Xiao-Ming Chen

Biodiversity endows similar species with subtle differences in composition, microstructure, and surface chemistry, making biomass a promising precursor to control the resulting active structure for heterocatalysis. Here, it is shown that *Tremella fuciformis* (*Tfu*), possessing an abundant porous structure and favorable metal affinity, is favorably serves as a precursor for confining uniform metal nanoparticles, by comparing the chemical characteristics of six varieties of agarics. The modest size of Co in the *Tfu* derived composite, Co@NPC-*Tfu* (NPC = N, P co-doped carbon), is suitable for in situ semi-oxidation during oxygen evolution reaction (OER), forming a stable core-shell structure of $Co_3O_4@Co$. Thus, Co@NPC-*Tfu* can be used as a state-of-the-art electrocatalyst for OER with an overpotential of 213.6 ± 4.1 mV at 10 mA cm^{-2}, and a significant turnover frequency of 3.21 s^{-1} at 300 mV, benefitting from the optimum trade-off between the atom utilization and electrical conductivity. Operando spectroscopy and theoretical calculations unveil the occupied state modulation of the robust carbon-bonded PO_x groups, which optimizes the intermediate adsorption to accelerate OER kinetics. Moreover, *Tfu* derived Ni@NPC-*Tfu* can be also prepared as a high-performance hydrogen evolution reaction electrocatalyst, which can be utilized for efficient overall water splitting coupled with Co@NPC-*Tfu*.

1. Introduction

Electrocatalytic water splitting by renewable electricity is a promising way of hydrogen production and resolving the increasingly serious environmental pollution and energy crisis.[1] Currently, researchers are devoted to develop inexpensive and efficient non-precious metal electrocatalysts to solve the commercialization limitation of noble metal ones, especially to overcome the kinetically sluggish oxygen evolution reaction (OER) on anode. Carbon supported transition metal nanoparticles (TMNs@C) are hot as newly electrocatalytic materials due to their intrinsic large specific surface areas, excellent conductivity, activity, and stability.[2] The carbon sources can be divided into organic carbon sources (amines,[3] alkanes[4] and halogenated organics,[5] etc.) and inorganic/hybrid carbon sources (graphene,[6] carbon nanotube[7] or metal-organic frameworks (MOFs),[8] etc.). The carbonization processes of organic carbon sources are rather complex and hard to regulate the final morphologies, which usually require special preparation techniques and always generate by-products. Inorganic/hybrid carbon sources have advantages since they can keep the morphologies of the precursors and achieve precise control of micro-nano structures, yet they are limited by their exorbitant prices as well as the difficulty of scaling preparation.[9]

The particle sizes of TMNs are of vital importance to their electrocatalytic performance.[10] Generally, TMNs will be easily oxidized into the corresponding metal oxides with higher active yet lower electrical conductivity on their surface especially under alkaline conditions and/or oxidation bias potential. When the particle size is too small, such oxidations tend to be exhaustive, leading to a high atom utilization rate of the active sites but a decreased conductivity. On the contrary, only superficial surface oxidations can occur if the size is too large, as a consequence, the atom utilization is relatively low. When the size of TMNs is enjoyable, it would be possible to form a semi-oxide core-shell structure (appropriate metal oxide on the shell layer and protect the metal in core from further oxidation), which be conducive to electrocatalytic performance with the favorable

J. Zhang, R.-Z. Sun, X.-F. Zhang, X.-Y. Zhu, L.-H. Yu, L.-Y. Guo, M.-L. Liu, L. Guo, L.-M. Cao, C.-T. He
Key Lab of Fluorine and Silicon for Energy Materials
and Chemistry of Ministry of Education, and College of Life Science
Jiangxi Normal University
Nanchang 330022, P. R. China
E-mail: hct@jxnu.edu.cn

J.-X. Wu, X.-M. Chen
MOE Key Laboratory of Bioinorganic and Synthetic Chemistry
School of Chemistry
Sun Yat-Sen University
Guangzhou 510275, P. R. China

Y.-H. Dou
Shandong Institute of Advanced Technology
Jinan 250100, P. R. China

**ADVANCED
SCIENCE NEWS**

www.advancedsciencenews.com

**ADVANCED
FUNCTIONAL
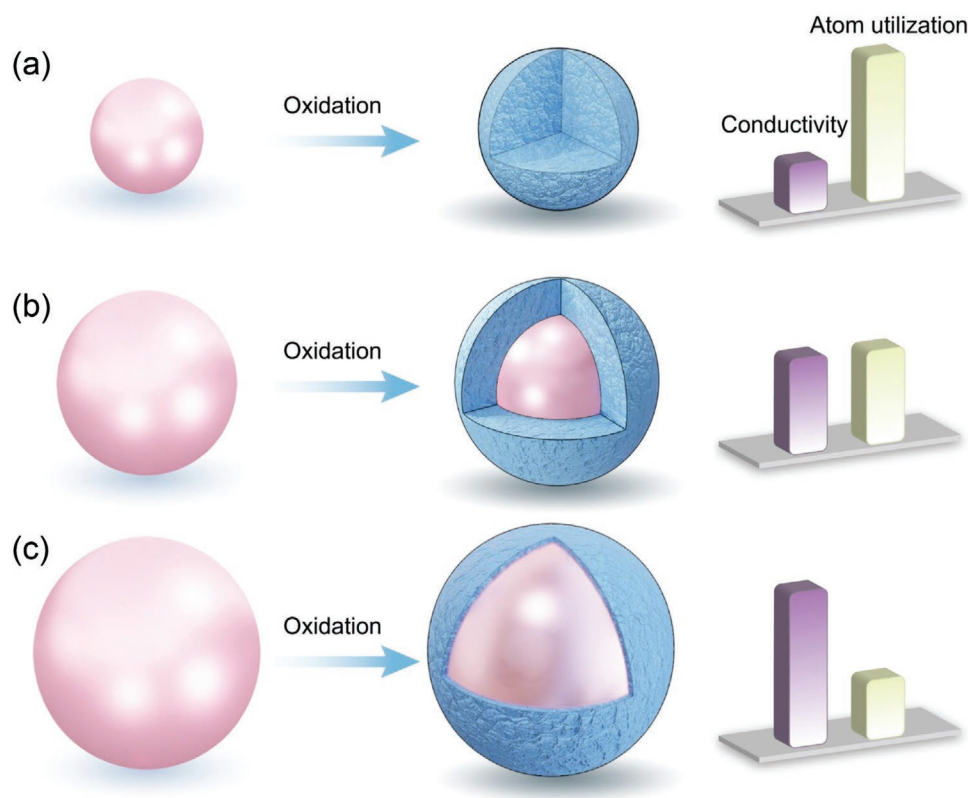MATERIALS**

www.afm-journal.de

Figure 1. Different oxidation types on metal nanoparticles with different sizes and the corresponding effects on the conductivity and atom utilization ratio: a) full oxidation, b) semi-oxidation, and c) surface oxidation.

conductivity and atom utilization (**Figure 1**). On the other hand, uncontrollable particle sintering/agglomeration of TMNs@C is usually difficult to be avoided, though that reducing the particle sizes and increasing the dispersion will make the catalysts more active. In order to obtain stable nanoparticles with desired sizes, porous molecule-based confinement has been proved to be an effective strategy recently. The unique space and coordination confinements of porous molecule-based materials, such as MOFs,[11] covalent organic frameworks (COFs),[12] and porous organic polymers (POPs),[13] etc., are conducive to prepare uniform nanoparticles with specific sizes. Besides, the organic wraps or carbon supports formed in situ serve as the electronic regulators and structural protectors, thereby leading to electrocatalysts with superior performance.

Biomass is a natural resource with a wide range of sources, low price, and renewability. Due to the rich carbon content and unique micro-nano-structure, biomass-derived carbon-based materials have shown unique advantages in heterocatalysis.[14] Similar to MOFs, COFs, or POPs, abundant N- or O-containing organic functional groups (from proteins and carbohydrates, etc.) in biomass can coordinate and confine metal ions/compounds, meanwhile the specific porous structures can provide effective confinement space. Besides, the heteroatoms (e.g., N, P, and S) rich in biomass can be doped into the carbon substrate in situ during the carbonization process, and benefit to adjust the electronic structure and then affect the catalytic performance.[15] Furthermore, biomass can skip the complicated synthesis processes, being conducive to the large-scale preparation.

Although a variety of biomasses have been used to prepare TMNs@C for energy catalysis, such as rose,[16] duckweed,[17] yeast,[18] and carrot.[19] However, most supported nanoparticles are purely large and of uneven sizes, which may greatly affect the catalytic performance. Moreover, in-depth studies on how different varieties of biomass affect the structures and activities of the catalysts, as well as their corresponding catalytic mechanisms remain great challenge. Agaric, a kind of worldwide abundant fungi, is cheap, rich in phosphorus (could be directly used as P source), and easy to be scalable produced. It possesses a 3D network structure, plentiful chitin and super high water absorption capacity, which make it promising as a precursor to prepare TMNs@C with excellent performance.[20] Considering the biological diversity, we selected six different varieties of agarics, *Tremella fuciformis* (*Tfu*), *Auricularia cornea* (*Aco*), *Auricularia nigricans* (*Ani*), and three kinds of *Auricularia auricular* (*Aau*) from different origins (Figure S1, Supporting Information), as precursors to prepare N and P co-doped carbon supported Co nanoparticles (denoted as Co@NPC-*γ*, *γ* = *Tfu*, *Ani*, *Aco*, *Aau*, *Aau*(Q), and *Aau*(F), NPC = N, P co-doped carbon). Through comparison, we found that the biodiversity had significant effects on the sizes and activities of their derived nanoparticles. Among them, the size of TMNs in Co@NPC-*Tfu* was modest for in situ semi-oxidation (ISSO) to form a stable core-shell structure. Thus, Co@NPC-*Tfu* exhibited the optimum OER performance, surpassing the benchmark RuO$_2$ and others reported Co or CoOx based electrocatalysts. Operando spectroscopic technology and DFT calculations revealed that the robust

carbon-bonded PO*x* groups derived from the phosphorus source in agaric also played an important role on the OER processes. This simple, low-cost, and scalable agaric-derived method can be easily extended to other transition metals. For instance, Ni@NPC-*Tfu* was successfully synthesized and exhibited remarkable hydrogen evolution reaction (HER) performance, which, being coupled with anode electrocatalyst of Co@NPC-*Tfu* into an overall water electrolysis device, merely needed a cell voltage of 1.53 V to drive a current density of 10 mA cm^{-2}.
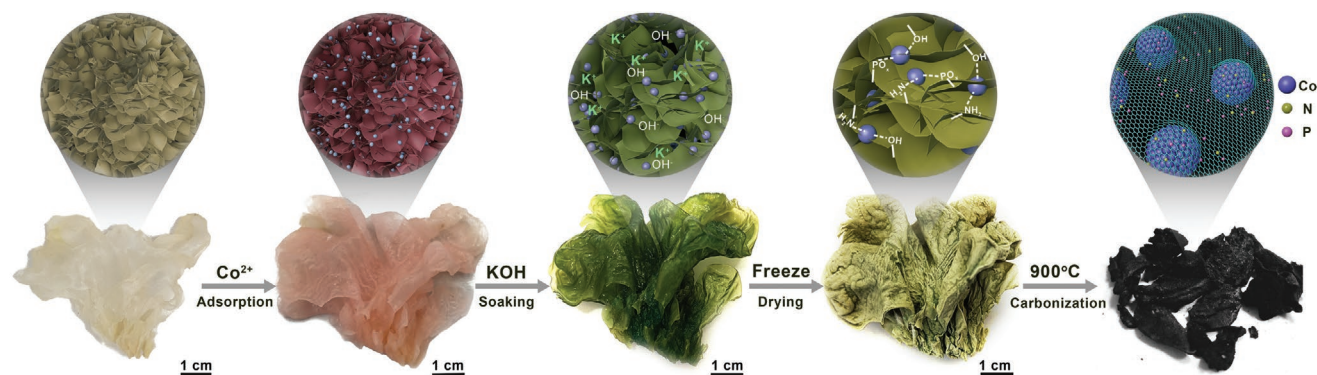
2. Results and Discussion

2.1. Size and Component Modulations by Biodiversity

All the agaric-derived N, P, and Co co-modified porous carbon nanosheets were synthesized by a simple adsorption-carbonization method (**Scheme 1**). Take the *Tfu* as an example, first, *Tfu* was soaked in cobalt nitrate solution and the color was changed to pink as well as the volume was expanded by ≈50%. Then the mixture was further treated with KOH solution and the color was changed to green (Figure S2, Supporting Information). Finally, after dehydration by freeze-drying, the sample was pyrolyzed at 900 °C under N$_2$ to generate the Co@NPC-*Tfu*. By this method, catalysts can be synthesized simply and in large quantities. For instance, we can prepare ≈10 g Co@NPC-*Tfu* with 45 g *Tfu* per time under our laboratory conditions (Figure S3, Supporting Information). It is worth noting that the cost of Co@NPC-*Tfu* is only ≈0.55 $ g^{-1} (Table S1, Supporting Information), being 1/277 of commercial RuO$_2$ (152.6 $ g^{-1}, from Aladdin).

As shown in the scanning electron microscopy (SEM) and transmission electron microscopy (TEM) images, although the microscopic morphology of various agarics after carbonization are similar, all of them have perfectly inherited interconnected 3D nanostructure, but there are subtle differences among different kinds of agarics. Co@NPC-*Tfu* possesses the fluffiest and porous network constructed by ultrathin nanosheets compared with other samples (**Figure 2**a). Co@NPC-*Ani*, *Aau*, *Aau*(Q), and *Aau*(F) also consist of lamellar-crossing porous networks yet look slightly thick and denser. Peculiarly, Co@NPC-*Aco* displays villous nanowires on the top of one side (Figure S4a, Supporting Information). The TEM images show that Co@NPC-*Tfu*, *Aau*, *Ani*, *Aco*, *Aau*(Q), and *Aau*(F) consist of Co nanoparticles that are encapsulated within carbon matrices. Interestingly, the distribution of Co NPs on Co@NPC-*Tfu* is the most uniform with the smallest average particle size of 9.7 nm (Figure 2b; Figure S4b, Supporting Information). Elemental mappings from energy dispersive X-ray spectrometry (EDS) revealed that C, N, P, and Co elements are homogeneously distributed in all the samples (Figure 2c; Figure S4c, Supporting Information). HRTEM images showed legible lattice fringes with a pitch of ≈0.204 nm corresponded to the (111) facets of Co crystal, confirming the formation of Co nanoparticles, and the Co nanoparticles are completely encapsulated by few-layers of carbon shells (Figure 2d; Figures S4d,S5, Supporting Information).[21] Besides, all the materials possessed very small thickness ranges from 2.7 to 4.3 nm tested by atomic force microscope (AFM), among which Co@NPC-*Tfu* was the thinnest while Co@NPC-*Aau* was the thickest (Figure 2e; Figure S6, Supporting Information). The ultrathin morphology of the Co@NPC-*Tfu* should have a positive effect on the electron transport in electrocatalysis.[22]

The surface electronegativity of *Tfu* was the strongest among all varieties since the lowest zeta potential of −21.9 ± 0.2 mV, which was beneficial for capturing and anchoring positively charged metal cations, resulting the smallest and uniform metal nanoparticles in Co@NPC-*Tfu* (Figure 2f). The architectures of samples after carbonization were further investigated via nitrogen sorption (Figures S7,S8, Supporting Information). The sorption isotherms showed that Co@NPC-*Tfu* owns the largest BET specific surface area (437 m^2 g^{-1}), being consistent with the observation of SEM. Interestingly, all of the samples exhibited uniform micropores with narrow size range from 0.8 to 1.2 nm (Co@NPC-*Aau* and Co@NPC-*Ani* even showed unimodal distributions), which were rarely observed in biomass derived carbon-based materials.[23] Raman spectra were further performed to investigate the structures of carbon matrixes (Figure S9, Supporting Information). Co@NPC-*Tfu* (0.97) and Co@NPC-*Aco* (1.01) possessed larger I_D/I_G values than other materials, suggesting the presence of more defects and/or heteroatom dopings, being conducive to expose more active sites and optimize the electronic structures.[24] The crystal phases of these materials were analyzed by powder X-ray diffraction (PXRD), and all of samples have a broad diffraction peak at 26.3°, which can be

Scheme 1. Schematic illustration of the synthesis process for Co@NPC-*Tfu*.

**ADVANCED
SCIENCE NEWS**

www.advancedsciencenews.com

**ADVANCED
FUNCTIONAL
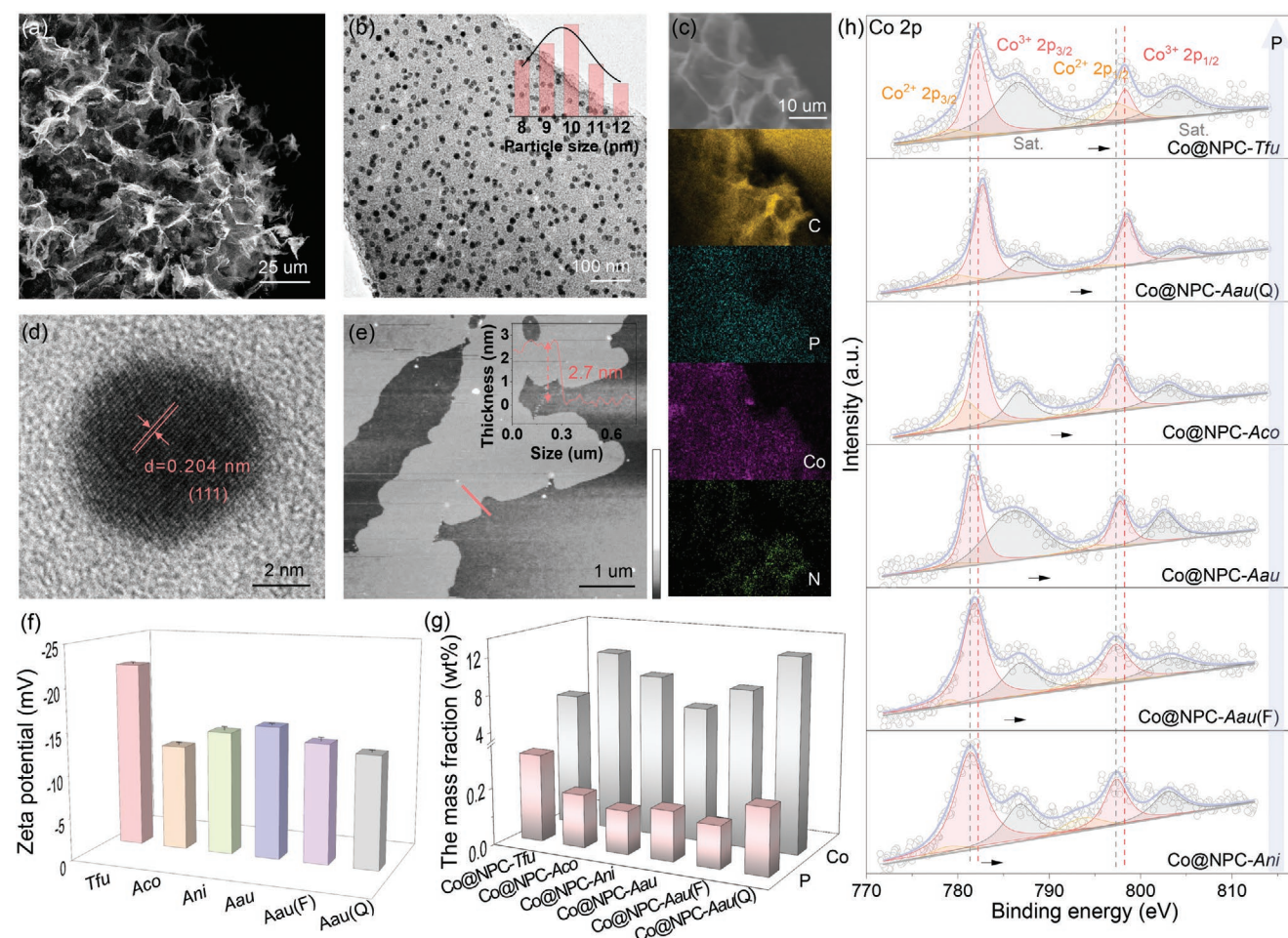MATERIALS**

www.afm-journal.de

Figure 2. Morphology characterizations: a) SEM image, b) TEM image (inset: particle-size distribution), c) elemental mappings, d) HRTEM image, and e) AFM image of Co@NPC-*Tfu*. f) Zeta potential of various agarics (error bars estimated from three experimental repetitions). g) The P and Co contents and h) Co 2p XPS spectra of Co@NPC-*Tfu*, *Aco*, *Ani*, *Aau*, *Aau*(F), and *Aau*(Q), respectively.

attributed to (002) planes of graphite carbon (JCPDS card no. 41-1487). Besides, there were three diffraction peaks, located at 44.2°, 51.4°, and 76.0°, corresponding to the (111), (200), and (220) crystal facets of Co, respectively (JCPDS card no.15-0806; Figures S10,S11, Supporting Information).

Through the inductively coupled plasma-optical emission spectrometry (ICP-OES) measurements, the accurate elemental contents of P and Co in this series of samples range from 0.14 to 0.3 wt%, and 6.25 to 12.69 wt%, respectively (Figure 2g). Among them, the content of P in Co@NPC-*Tfu* is the largest (0.3 wt%), which foreshadows more active defect sites and stronger electronic transfer in this material. Nevertheless, the content of Co is the lowest (6.25 wt%), suggesting Co@NPC-*Tfu* may have higher mass activity in electrocatalysis. In order to reveal the bonding configuration of P, Fourier transform infrared (FT-IR) spectra of all the samples were carried out. Two characteristic peaks at 1124 and 1068 cm^{-1} can be obviously observed, corresponding to the P—C and P—O stretching, respectively (Figure S12, Supporting Information).[25] The detailed chemical states of elements were characterized by X-ray photoelectron spectroscopy (XPS). It can be seen that all samples contain C, P, N, O, and Co elements, as well as have very similar

high-resolution XPS spectra for each element (Figures S13,S15, Supporting Information).[26] The C 1s fine spectrum shows three peaks with binding energies at 286.5, 285.7, and 284.8 eV, which can be assigned to C—N, C—P and C=C, respectively (Figure S12, Supporting Information).[27] In the high-resolution P 2p spectra, the bonding species of P—C located around 133.5 eV are still obvious although the other signal strength is weak (Figure S14, Supporting Information).[28] The C 1s and P 2p spectra indicate that the P atoms were mainly doped into the carbon matrix to form robust covalent bonded POx groups, being consistent with the EDS and FT-IR results. Interestingly, the binding energy of Co in the high-resolution spectrum of Co 2p corresponded to the phosphorus content in samples. As the phosphorus content increased, the binding energy of the Co species was positively shift, implying the carbon-bonded POx groups can promote the electron transfer from Co, creating an more electron-deficient feature on the Co of Co@NPC-*Tfu*, which could facilitate the catalytic performance (Figure 2h). However, the binding energy of Co did not shift in Co@NPC-*Tfu* with different metal loadings, further confirming that the electronic structure of Co is mainly affected by the content of P rather than the size of nanoparticle (Figure S16, Supporting

**ADVANCED
SCIENCE NEWS**
www.advancedsciencenews.com

**ADVANCED
FUNCTIONAL
MATERIALS**
www.afm-journal.de

Information). To sum up, the advantages of *Tfu* in microstructure, surface electronegativity, and phosphorus content are conducive to the confinement of metal precursors, the size modulation of nanoparticles, and the electronic regulation of Co, respectively, all of which will contribute positively to the catalytic performance of Co@NPC-*Tfu*.

2.2. Electrocatalytic Activity Evaluation

The electrocatalytic performances of the catalysts were first evaluated by linear sweep voltammetry (LSV), showing that Co@NPC-*Tfu* exhibited the best OER performance between control samples (Figure S17, Supporting Information). At the current density of 10 mA cm^{-2}, Co@NPC-*Tfu* showed the lowest overpotential of 245.7 ± 1.5 mV on glassy carbon electrode (GCE), being lower than other Co$_x$@NPC-*Tfu* (Figure S18, Supporting Information), as well as those of Co@NPC-*Aco* (348.7 ± 1.5 mV), Co@NPC-*Ani* (404.3 ± 15.6 mV), Co@NPC-*Aau* (296.7 ± 0.6 mV), Co@NPC-*Aau*(F) (318.7 ± 2.1 mV), Co@NPC-*Aau*(Q) (370.3 ± 8.0 mV), and the benchmark RuO$_2$ (333.3 ± 3.5 mV). The Tafel slope of Co@NPC-*Tfu* was 63.9 ± 1.3 mV dec^{-1}, which also lower than other catalysts (**Figure 3**a,b; Figures S19,S21, Supporting Information). We further analyzed the relationships between $\Delta\eta/\Delta\log|j|$ and current densities, while smaller $\Delta\eta/\Delta\log|j|$ ratio needs less overpotential when current density increases, which has better catalytic performance (Figure 3c). When the current density was lower than 60 mA cm^{-2}, the ratios for Co@NPC-*Tfu* and RuO$_2$ were not far apart. However, when up to the higher current density (e.g., 120 mA cm^{-2}), the ratio for Co@NPC-*Tfu* (182.8 ± 17.7 mV dec^{-1}) was significantly much lower than that of RuO$_2$ (425.9 ± 11.6 mV dec^{-1}), indicating that Co@NPC-*Tfu* could work even better for high-current-density. It is worth noting that the overpotential of Co@NPC-*Tfu* on GCE is remarkably smaller than the reported values for cobalt/cobalt oxide-based electro-catalysts and other single metal high-performanced OER electrocatalysts, and serve as one of the state-of-the-art OER electrocatalysts (Figure 3d; Tables S2,S3, Supporting Information). Considering the substrate effect, we also tested the OER performance of Co@NPC-*Tfu* on carbon cloth (CC), which merely needed an overpotential of 213.6 ± 4.1 mV at 10 mA cm^{-2}, and after a 24 h chronopotentiometry test, the potential only increased by 3.2% (Figure 3f). By detecting the cobalt and phosphorus contents in the electrolytes after 100 and 1000 cycles of CV, we found changes of both P and Co contents in the electrolytes were negligible after the electrolysis process, further confirming the stability of Co@NPC-*Tfu* and the carbon-bonded PO$_x$ groups (Table S4, Supporting Information). Materials with lower charge transfer resistance (R_{ct}) will accompany with better catalytic performance, so we carried out electrochemical impedance spectroscopy (EIS) measurements. It can be found that Co@NPC-*Tfu* exhibited the fastest electron transfer since its much smaller R_{ct} value compared with other reference catalysts (Figure S22, Supporting Information). To clearly reflect the electrocatalytic activities of different catalysts, the electrochemically active surface area (ECSA) is assessed. The ECSA was responded by the double-layer capacitance (C_{dl}), which derived from cyclic voltammetry (CV) by different scan speed from 60 to
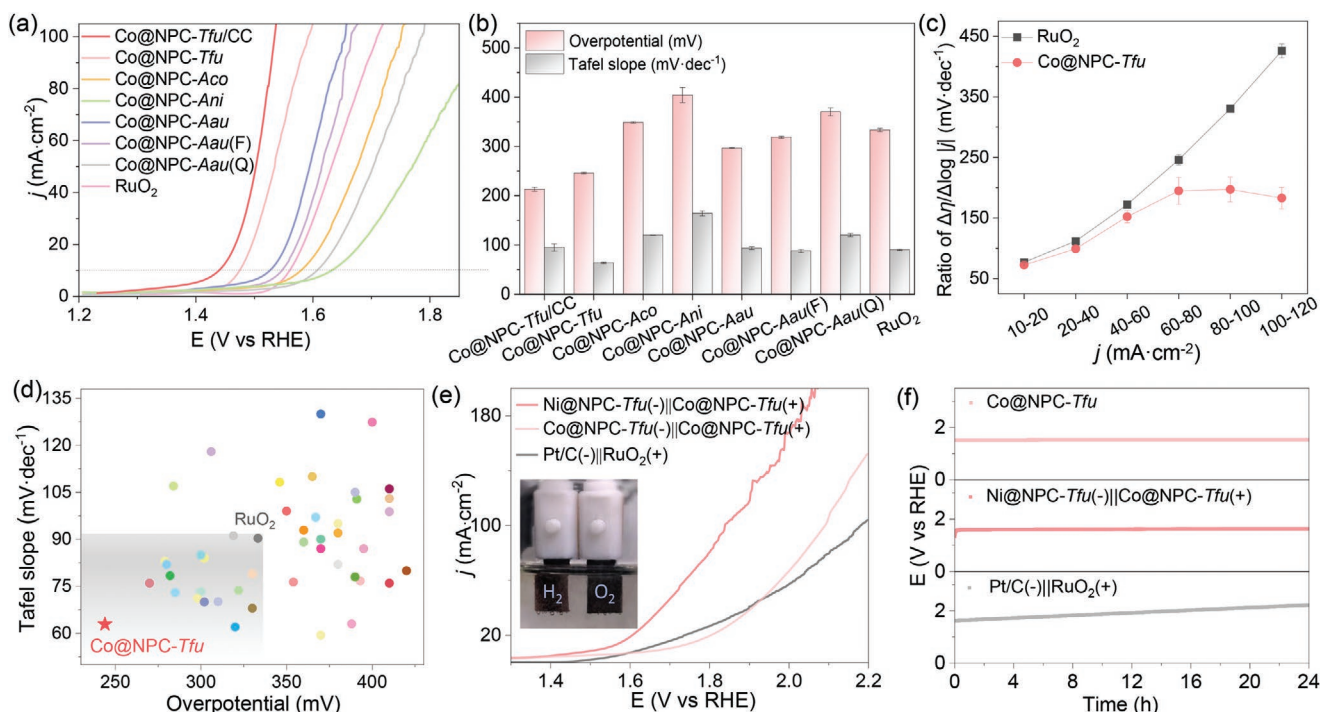

Figure 3. Water splitting performances: a) OER polarization curves. b) Overpotentials at 10 mA cm^{-2} and the corresponding Tafel slopes with error bars. c) Ratios of $\Delta\eta/\Delta\log|j|$ at different current density intervals. d) Comparing the overpotential at 10 mA cm^{-2} and corresponding Tafel slope with other Co or CoO$_x$ based electrocatalysts. e) Polarization curves of overall water splitting (inset: the photograph of water splitting device showing gas bubbles on the electrodes). f) Long-term durabilities testing by chronopotentiometry.

**ADVANCED
SCIENCE NEWS**
www.advancedsciencenews.com

**ADVANCED
FUNCTIONAL
MATERIALS**
www.afm-journal.de

140 mV s^{-1} in a nonfaradic region. The C_{dl} of Co@NPC-*Tfu* (2.83 mF cm^{-2}) is higher than those of other agaric derived catalysts, indicating that Co@NPC-*Tfu* owns largest exposed active specific area, which is favorable to the OER (Figures S23,S24, Supporting Information). Furthermore, Co@NPC-*Tfu* exhibited an excellent turnover frequency (TOF) of 3.21 s^{-1} at an overpotential of 300 mV and an almost 100% Faradaic efficiency for OER (Figures S25,S26, Supporting Information).

To verify the universality of our method, we also prepared *Tfu*-derived Ni-N-P implanted porous carbon nanosheets to serve as an HER catalyst (Ni$_x$@NPC-*Tfu*, where x represents the concentration of Ni), and all samples of Ni$_x$@NPC-*Tfu* possessed the same Ni phase without other crystalline impurities (Figure S27, Supporting Information). LSV polarization curves showed that Ni@NPC-*Tfu* has the best HER performance among them even much better than Co@NPC-*Tfu*, with a low overpotential of 140.3 ± 3.2 mV at current densities of 10 mA cm^{-2} and a small Tafel slope of 98.9 ± 6.2 mV dec^{-1} (Figures S28,S30, Supporting Information). Besides, an overall water electrolysis device was constructed with the Co@NPC-*Tfu* and Ni@NPC-*Tfu* served as the anode and cathode, respectively. Impressively, the electrolyzer only needs a cell voltage of 1.53 V, being 100 mV lower than that of Pt/C(−)‖RuO$_2$(+) and 160 mV lower than that of Co@NPC-*Tfu*(−)‖Co@NPC-*Tfu*(+) at 10 mA cm^{-2} (Figure 3e). Moreover, the electrolyzer of Ni@NPC-*Tfu*(−)‖Co@NPC-*Tfu*(+) possessed a better durability (collapsed by 2.6%) at 10 mA cm^{-2} for at least 24 h, while that of Pt/C(−)‖RuO$_2$(+) was reduced by 32.2% at the same conditions (Figure 3f).

2.3. In Situ Semi-Oxidation and Electrocatalytic Mechanisms

After 24 h of electrolysis, we found that the cobalt nanoparticles on Co@NPC-*Tfu* became a core-shell structure (**Figure 4**a). In the HRTEM image, we can clearly see that the lattice fringe of the core structure corresponds to (111) facet of Co phase, while the lattice fringe of shell structure corresponds to (220) facets of Co$_3$O$_4$, the thickness of the cobalt oxide on the outer shell was ≈4 nm, and the core diameter was ≈7 nm (Figure 4b). After the reaction, the average particle size of the nanoparticles is ≈15 nm, being about 50% larger than that of original cobalt nanoparticles, which is caused by the lattice expansion after the insertion of oxygen atoms.

We further monitored the changes of the electrocatalyst by performing quasi-operando PXRD under a constant current and different voltages, the results illustrated that the diffraction peaks of Co$_3$O$_4$ began to appear after just 1 min galvanostatic electrolysis, then the diffraction of metallic cobalt gradually weakened, and that of Co$_3$O$_4$ gradually enhanced, till reaching a transient stability at 4 min, but metallic cobalt still existed. Further prolonging the time of electrolysis, the crystallinity of the shell became worse and the peak intensity became weaker due to that the oxidation reactions caused more and more structural defects and/or disorders on the surface (Figure 4c).[29] Interestingly, the Co$_3$O$_4$ was very easily formed when the voltage is only 0.2 V from the results of quasi-operando PXRD under constant voltage electrocatalysis (Figure S31, Supporting Information). It is worth mentioning that the diffraction peaks of cobalt nanoparticles have no significant change with further prolonged

electrolysis time or increase of the voltage, indicating that the cobalt nanoparticles in the inner core was not further oxidized after the oxidation reaches an equilibrium, thus forming a stable core-shell structure (Figure 4d). In contrast, the smaller cobalt nanoparticles on Co$_{0.05}$@NPC-*Tfu* were completely oxidized to Co$_3$O$_4$ and the larger ones on Co@NPC-*Aau*(F) remained almost no changed except the surface became amorphous after the same electrocatalysis (Figure S32, Supporting Information). In these two later cases, either poor conductivity or low atom utilization would reduce the catalytic activity. Obviously, an appropriate nanoparticle size should be significant to the formation of such a stable core-shell structure, which is not only easy to form an oxide shell, but also effectively prevent the complete oxidation when the shell has formed. This special core-shell structure is beneficial to form new highly active sites while maintaining the advantage of high electrical conductivity of cobalt nanoparticles.

To deeply understand the electronic effect of the phosphorus-enriched carbon on the cobalt oxide for OER, operando spectroscopic technology and density functional theory (DFT) calculations were performed to dissect the electrocatalytic mechanism of Co@NPC-*Tfu*. The operando Raman spectra were collected during a gradual increase in the potential, to study the activated structure.[30] The bands at 191, 484, 523, 620, and 690 cm^{-1}, owed to the F_{2g}, E_g, F_{2g}, F_{2g}, and A_{1g} modes typical for Co$_3$O$_4$, further confirmed that the surface of Co nanoparticles was oxidized to Co$_3$O$_4$ easily by only a voltage of 0.2 V, being well consistent with the results of quasi-operando PXRD.[31] At the onset of oxygen evolution at ≈0.6 V, an additional band at 503 cm^{-1} for the OH stretching mode of Co−OH on the Co$_3$O$_4$ surface appeared and the intensity increased with rising voltage (**Figure 5**a).[32] After the reaction, the bands of Co$_3$O$_4$ still existed, but that of hydroxyl disappeared, indicating that the structural transformation was reversible, the adsorption of hydroxyl was a necessary intermediate process, and there is no formation of CoOOH, which is consistent with the previously reported results.[33] Furthermore, we recorded the operando ATR-SEIRAS (attenuated-total-reflection surface enhanced infrared adsorption spectroscopy) of Co@NPC-*Tfu* during different periods of OER at a constant catalytic voltage of 0.50 V versus SCE (Figure 5b).[34] Three peaks at 1087, 1451, and 1745 cm^{-1} attributed to P−O, C−O, and C=O, respectively, became stronger with time prolongation, indicating an associated oxidation of the carbon matrixes during OER. It is worth noting that the enhancement of the P−O bond implied that the sp^2-type P groups bonded in the carbon would be converted to sp^3-type PO$_x$, which should better regulate the electronic structure of the active center. The progressively rising peak of −OH stretching at 3682 cm^{-1} indicated the increased surface hydrophilicity, as well as the enhanced absorption of water or hydroxyl on the catalyst surface.[35]

DFT calculations were further conducted based on periodic surface models of pure Co$_3$O$_4$, N-doped carbon modified Co$_3$O$_4$ (Co$_3$O$_4$@NC), PO, N-codoped carbon modified Co$_3$O$_4$ (Co$_3$O$_4$@NC-PO), and PO$_2$, N-codoped carbon modified Co$_3$O$_4$ (Co$_3$O$_4$@NC-PO$_2$ and Co$_3$O$_4$@NC-PO$_2$-b for different N positions), respectively (Figure 5c,d; Figure S33, Supporting Information).[36] The surface model based on Co$_3$O$_4$ exhibits di-μ-oxo-bridged octahedral metal ions, which similar to the local coordination
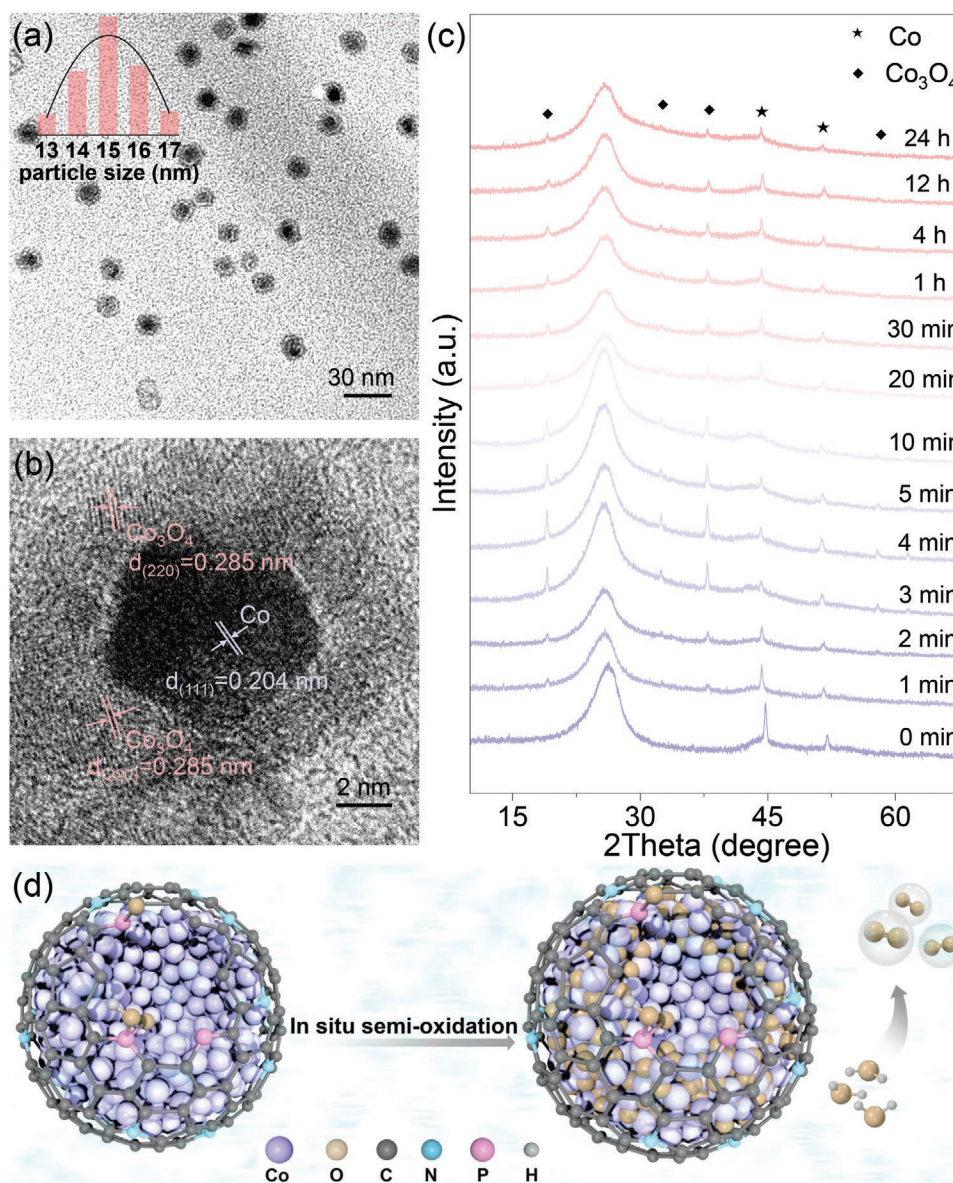
Figure 4. Characterization of the in situ semi-oxidation: a) TEM (insets: particle-size distributions) and b) HRTEM images of Co@NPC-*Tfu* after OER electrocatalysis. c) Quasi-operando PXRD monitoring of Co@NPC-*Tfu* under constant current with different time. d) Schematic diagram of atomic models in perspective view of Co@NPC-*Tfu* before and after OER electrocatalysis (a small gap of carbon shell and the metal core were opened for clarity).

environment of the active Co site in CoOOH, and the protonation of O on the surface part to OH have been considered in DFT calculations.[37] From the calculated energy profiles, we found that the metal sites on Co_3O_4 surface exhibited stronger affinity to the oxygen species,[38] especially for the intermediate O* (ΔG_{O*} = 1.635 eV), and then led to the rate-determining-step (RDS) of OOH* formation with a rather high energy barrier of 1.793 eV. When N-doped carbon was coupled with the metal oxide, the ΔG_{O*} can be obviously enhanced to 1.877 eV for easier OOH* formation as the RDS decreased to 1.692 eV. Interestingly, the oxygen adsorption was further weakened (ΔG_{O*} = 2.296 eV) and the RDS was changed to the formation of O* with lower energy barrier of 1.462 eV, when a sp³-PO_2 group was grafted to the N-doped carbon. However, if the functional group

was changed to sp²-PO, the RDS energy was, instead, raised up due to the weak oxygen affinity. Nevertheless, it was still much better than those of Co_3O_4 and Co_3O_4@NC (Figure 5c). It is worth noting that the positions of heteroatoms had significant effects on the activity of the catalysts, and for instance, that the N and P atoms connected directly (Co_3O_4@NC-PO_2-b) was not as good as that separated by a carbon atom (Co_3O_4@NC-PO_2). Through in-depth analyzing the integrated partial density of state (PDOS) of Co active site in each catalyst, we found that the strength of O* affinity was almost linear with the metal occupied state (MOS), which represented the total number of states (electrons) up to the Fermi level (Figure S34, Supporting Information) and also reflected the electron density on the metal sites. The higher the MOS, the stronger adsorption of O with smaller
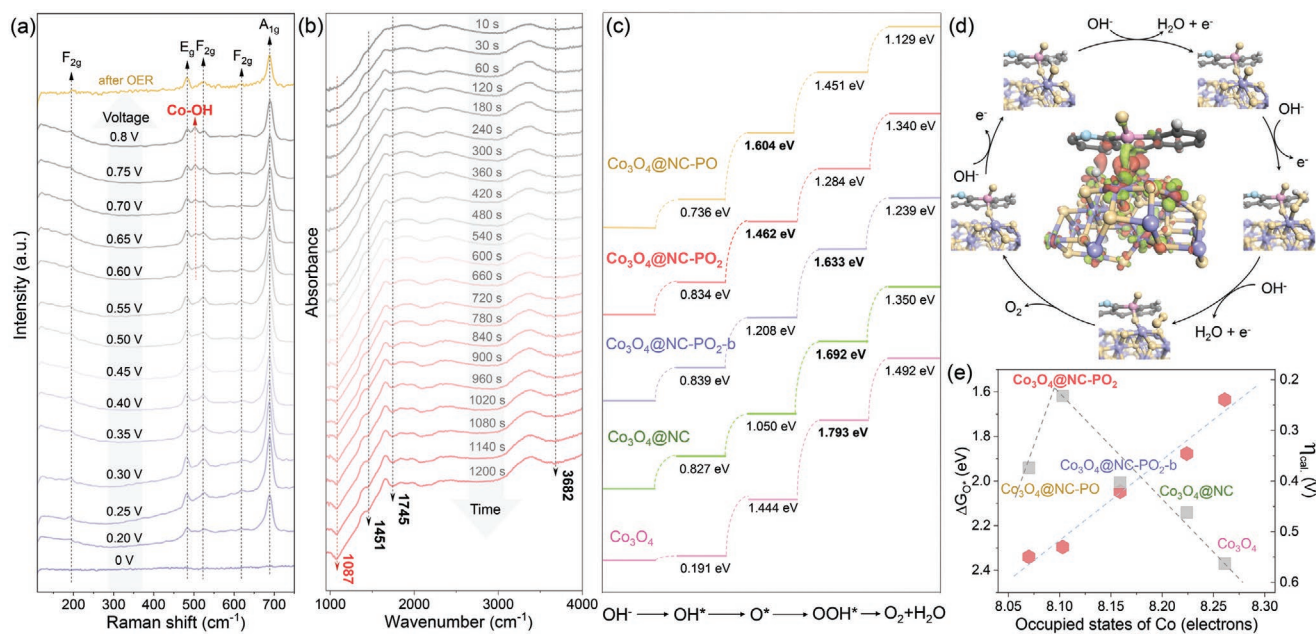
Figure 5. Operando spectroscopic investigations and DFT calculations: a) Operando Raman and b) operando ATR-SEIRAS of Co@NPC-*Tfu* during OER electrocatalysis. c) Gibbs free energy profiles for OER of different Co_3O_4-carbon composite models. d) Electron density difference (the red and green regions indicate electron accumulation and depletion, isovalue = 0.05) after the N, P co-doped carbon layer combined with Co_3O_4 (central inset) and OER mechanism with optimal conformations of the Co_3O_4@NC-PO$_2$ surface model (the hydrogen atoms on the surface have been hided for clarity). e) Volcano plot of calculated overpotential and scaling relation between ΔG_{O*} and the occupied states of Co derived from their integrated PDOS profile.

ΔG_{O*}. After compositing with the carbon matrix, the MOS has decreased to result a weaker O adsorption. This means that electrons would transfer from the metal oxides to the P, N-codoped carbon matrix, which can be visualized by the electron density difference plot of Co_3O_4@NC-PO$_2$ (central inset in Figure 5d). Moreover, based on the famous Sabatier principle, neither too strong nor too weak intermediate-adsorption is conducive to the activity. Thus, the MOS can be used as a descriptor to draw a volcano plot for predicting the activity of these composite catalysts (Figure 5e). Co_3O_4@NC-PO$_2$ located close to the volcanic peak due to a more balance MOS value compared with those of bare Co_3O_4 and P-free counterpart. These theoretical results were consistent with the XPS and electrocatalytic measurements.

3. Conclusions

In summary, a series of carbon-supported cobalt composite materials with controlled morphologies and nanoparticle sizes have been synthesized, benefitting from the biodiversity of agarics on compositions, microstructures, as well as surface chemical states. Among them, Co@NPC-*Tfu* possessed ultrathin nanosheets with modest Co particle size of ≈10 nm showed the optimum OER performance with overpotentials of 245.7 ± 1.5 mV on GCE and 213.6 ± 4.1 on CC at the current density of 10 mA cm^{-2}, surpassing the commercial RuO_2 and other reported Co-based electrocatalysts. HRTEM, quasi-operando PXRD, and operando Raman measurements unveiled the self-reconstruction of cobalt to cobalt oxides on the Co particle surface during OER. The results demonstrated that a judiciously selected precursor can help to regulate the size of nanoparti-

cles, which was in favor of ISSO to form a highly active shell structure while retaining the high electrical conductivity of the metallic core, achieving a stable and synergetic core-shell structure to greatly facilitate electrocatalytic oxygen evolution. Moreover, operando ATR-SEIRAS and DFT calculations revealed that the robust carbon-bonded PO$_x$ groups, derived from the phosphorus source in agaric, can effectively modulate the occupied states of the cobalt centers to optimize the adsorption of reactive oxygen intermediate, and further improve the final catalytic activity. Besides, *Tfu* also can be used as a precursor to fabricate HER electrocatalyst of Ni@NPC-*Tfu* for efficient overall water splitting with Co@NPC-*Tfu*, merely delivers low cell voltage of 1.53 V at 10 mA cm^{-2}. Our work not only proposes a low-cost and scalable method for preparation of porous carbon-supported metal nanomaterials with controllable morphology, but also provides new clue for screening suitable biomass for the construction of high-efficiency electrocatalysts.

4. Experimental Section

Material: In this work, 6 varieties of agarics were chosen that were common varieties on the market, which were widely grown and inexpensive, and suitable for using as raw materials for industry in the future. They belong to the same family and have basically the same composition, but were produced in different regions in China. *Tfu* was produced in Ningde City, Fujian Province. *Aco* was produced in Heze City, Shandong Province. Both *Ani* and *Aau* were produced in Jiaohe City, Jilin Province. *Aau* (F) was produced in Fang County, Hubei Province. *Aau* (Q) was produced in Mudanjiang City, Heilongjiang Province. All chemical reagents were purchased from Aladdin and used without further purification, except that Nafion was purchased from Macleans. KOH reagent used in electrochemical measurement was 99.99%

(semiconductor grade), and the resistivity of ultrapure water used in the whole work was ≈18.2 MΩ·cm^{-1}.

Preparation of Agaric-Derived Co@NPC and Ni$_x$@NPC-Tfu: 10 g different varieties of dried agarics were soaked in 400 mL Co(NO$_3$)$_2$ solution (0.1 M) for 24 h, then immersed in 0.1 M KOH for 24 h. After that, the samples were freeze-dried for 48 h with liquid nitrogen treatment. Finally, the dried products were pyrolyzed under N$_2$ atmosphere at 900 °C for 2 h at a heating rate of 5 °C·min^{-1}. The carbonized samples were collected and denoted as Co@NPC-*Tfu*, Co@NPC-*Aco*, Co@NPC-*Ani*, Co@NPC-*Aau*, Co@NPC-*Aau* (Q), and Co@NPC-*Aau* (F), respectively. *Tfu* was also soaked in Co(NO$_3$)$_2$ solution with various concentration denoted as Co$_x$@NPC-*Tfu* (x = 0.05, 0.2, 0.3, 0.4 M), where x represents the molarity of Co(NO$_3$)$_2$ solution. The preparation of Ni$_x$@NPC-*Tfu* was synthesized by using Ni(NO$_3$)$_2$ solution instead of Co(NO$_3$)$_2$ solution.

Material Characterization: The zeta potential of 6 varieties of agarics were characterized by an Omni Zeta Potential Analyzer (Brookhaven, USA). The phase structure was analyzed with a Rigaku MiniFlex600 X-ray diffractometer (PXRD, 45 kV, 15 mA, CuKα radiation). The morphology of the catalyst was characterized by Zeiss SEM and JEM2100F TEM. The content of Co and P was determined by the Agilent 7700 ICP-OES. The XPS data were collected on the Escalab 250Xi X-ray photo-electron spectrometer. Information of molecular structures and chemical bonds were determined by FT-IR (Nicolet 6700) and confocal Raman spectrometer (Raman, 532 nm excitation wavelength, Thermofisher Dxi). Electrochemical operando ATR-SEIRAS was measured by Nicolet iS50 equipped with an MCT detector cooled with liquid nitrogen and PIKE VeeMAX III variable angle ATR sampling accessory. Operando Raman was performed by Renishaw inVia with a wavelength of 532 nm, a 1800 g mm^{-1} grating, and an integration time of 30 s. AFM was conducted on Bruker Dimension ICON. Nitrogen sorption isotherms at 77 K were measured on Micrometrics ASAP2020 Plus instrument. In order to remove the remnant guest molecules, each sample (≈100 mg) was placed in the quartz tube and heated under high vacuum at 150 °C before sorption experiments. The specific surface areas and the corresponding pore size distribution curves were calculated using the BET and the Barrett–Joyner–Halenda method, respectively.

Electrochemical Measurement: Electrochemical workstation (CHI760E A19012b) was utilized to perform all electrochemical tests in 1.0 M KOH solution with a classic three-electrode system for both OER and HER, and the two-electrode system for overall water splitting. The electrolyte was purged with N$_2$ for 1 h to remove the dissolved gases completely before the electrochemical measurements. Both OER and HER tests were used saturated Hg/HgO electrode as the reference electrode, and a GCE coated with catalyst as working electrode. Platinum plate was used as counter electrode for OER, while carbon rod was used as counter electrode for HER. 5 mg of each catalyst, 30 μL of Nafion solution (10%), and 300 μL of water/isopropanol (V/V = 1:1) were mixed by ultrasonic for 1 h to prepare a catalyst ink, and 5 μL of ink was evenly spreaded onto a cleaned GCE (diameter of 3 mm). After carried out several cycles of CV tests on each electrode to initially activate the catalyst and make it reach a steady state, the LSV was used to study the linear polarization curve of the catalyst with a sweep rate of 10 mV s^{-1}, while a 90% iR correction was performed. The potential was calibrated against to the reversible hydrogen electrode (RHE) ($E_{RHE} = E + E_{Hg/HgO} + 0.0591 \times pH$). EIS was measured within a frequency scan range from 0.01 Hz to 100 kHz. 50 μL of above catalyst ink was also dropped on CC (0.4 cm^2) as working electrode to carry the OER, overall water electrolysis and durability test in 1.0 M KOH (mass loading of catalyst was 0.75 mg cm^{-2}). The TOF values were calculated using the following equation: TOF = $jA/(4 \times F \times n)$, where j, A, F, and n represent the current density, area of the electrode, faraday constant (96 485 C·mol^{-1}), and moles of catalysts, respectively. The actual yield of O$_2$ used in Faraday efficiency calculation was measured on a gas chromatography (Nexis GC-2030).

Computational Methods: The geometry optimizations, energy, and property calculations were all performed by spin-polarized density functional theory (DFT) with plane wave pseudo-potential method, as implemented in the Cambridge Sequential Total Energy Package (CASTEP) module integrated in Materials Studio. The OTFG ultrasoft pseudo-potentials and the Perdew–Burke–Ernzerhof within the generalized gradient approximation were selected to describe the exchange–correlation functional. The plane-wave energy cut-off was chosen as 30 Ry, and the Brillouin zone was sampled using k-points with 0.07 and 0.025 Å^{-1} spacing in the Monkhorst–Pack scheme for the geometry optimization and property calculation, respectively. Co$_3$O$_4$ and graphite crystal structures were adopted to build the periodical surface models. The (220) crystal facet was used in this work for simulating the exposed surface of Co$_3$O$_4$, which was observed in the PXRD and HRTEM results. A vacuum slab of 15 Å was added to isolate the interaction between periodic layers. The convergence criteria for the stress, self-consistent field iterations, atomic displacement, forces, and total energy were set to 5×10^{-2} GPa, 1×10^{-6} eV atom^{-1}, 1×10^{-3} Å, 3×10^{-2} eV Å^{-1}, and 1×10^{-5} eV atom^{-1}, respectively.

Adsorption energies of the OER intermediates (ΔE_i, i = OH*, O*, and OOH*) were calculated as the following formulas:

$$\Delta E_{OH*} = E_{OH*} - E_* - \left(E_{H_2O} - 1/2E_{H_2}\right) \tag{1}$$

$$\Delta E_{O*} = E_{O*} - E_* - \left(E_{H_2O} - E_{H_2}\right) \tag{2}$$

$$\Delta E_{OOH*} = E_{OOH*} - E_* - \left(2E_{H_2O} - 3/2E_{H_2}\right) \tag{3}$$

where, E represents the total energy derived from the above DFT calculations, and * denotes an active site of the catalyst. The Gibbs free energies of the OER intermediates (ΔG_i, i = OH*, O*, and OOH*) were calculated through corrected the adsorption energies with zero point energy (ZPE) and entropy (TS), using the formula: $\Delta G_i = \Delta E_i + \Delta ZPE_i - T\Delta S_i$.

Supporting Information

Supporting Information is available from the Wiley Online Library or from the author.

Conflict of Interest

The authors declare no conflict of interest.

Data Availability Statement

The data that support the findings of this study are available from the corresponding author upon reasonable request.

[1] a) W. J. Jiang, T. Tang, Y. Zhang, J. S. Hu, *Acc. Chem. Res.* **2020**, *53*, 1111; b) N. Selvam, L. Du, B. Xia, P. Yoo, B. You, *Adv. Funct. Mater.* **2020**, *32*, 2008190.

[2] X. Huang, T. Shen, T. Zhang, H. Qiu, X. Gu, Z. Ali, Y. Hou, *Adv. Energy Mater.* **2020**, *10*, 1900375.

[3] H.-P. Cong, X.-C. Ren, P. Wang, S. Yu, *Energy Environ. Sci.* **2013**, *6*, 1185.

[4] K. S. Novoselov, A. K. Geim, S. V. Morozov, D. Jiang, M. I. Katsnelson, I. V. Grigorieva, S. V. Dubonos, A. A. Firsov, *Nature* **2005**, *438*, 197.

[5] C. Morchutt, J. Bjork, S. Krotzky, R. Gutzler, K. Kern, *ChemComm* **2015**, *51*, 2440.

[6] Y. Shi, Y. Zhou, D. R. Yang, W. X. Xu, C. Wang, F. B. Wang, J. J. Xu, X. H. Xia, H. Y. Chen, *J. Am. Chem. Soc.* **2017**, *139*, 15479.

[7] X. T. Wang, T. Ouyang, L. Wang, J. H. Zhong, T. Ma, Z. Q. Liu, *Angew. Chem., Int. Ed.* **2019**, *58*, 13291.

[8] Z. Wang, W. Xu, X. Chen, Y. Peng, Y. Song, C. Lv, H. Liu, J. Sun, D. Yuan, X. Li, X. Guo, D. Yang, L. Zhang, *Adv. Funct. Mater.* **2019**, *29*, 1902815.

[9] a) Y. Meng, X. Huang, H. Lin, P. Zhang, Q. Gao, W. Li, *Front. Chem.* **2019**, *7*, 759; b) J. Wang, H. Kong, J. Zhang, Y. Hao, Z. Shao, F. Ciucci, *Prog. Mater. Sci.* **2021**, *116*, 100717.

[10] a) H. Wang, X. K. Gu, X. Zheng, H. Pan, J. Zhu, S. Chen, L. Cao, W. X. Li, J. Lu, *Sci. Adv.* **2019**, *5*, eaat6413; b) W. Xiao, W. Lei, M. Gong, H. Xin, D. Wang, *ACS Catal.* **2018**, *8*, 3237; c) X. F. Yang, A. Wang, B. Qiao, J. Li, J. Liu, T. Zhang, *Acc. Chem. Res.* **2013**, *46*, 1740.

[11] a) Q. L. Zhu, J. Li, Q. Xu, *J. Am. Chem. Soc.* **2013**, *135*, 10210; b) Y. Z. Chen, Q. Xu, S. H. Yu, H. L. Jiang, *Small* **2015**, *11*, 71; c) H. Liu, L. Chang, C. Bai, L. Chen, R. Luque, Y. Li, *Angew. Chem., Int. Ed.* **2016**, *55*, 5019.

[12] a) Y. Deng, Z. Zhang, P. Du, X. Ning, Y. Wang, D. Zhang, J. Liu, S. Zhang, X. Lu, *Angew. Chem., Int. Ed.* **2020**, *59*, 6082; b) S. Lu, Y. Hu, S. Wan, R. McCaffrey, Y. Jin, H. Gu, W. Zhang, *J. Am. Chem. Soc.* **2017**, *139*, 17082; c) H. C. Ma, C. C. Zhao, G. J. Chen, Y. B. Dong, *Nat. Commun.* **2019**, *10*, 3368.

[13] a) J. Mahmood, F. Li, S. M. Jung, M. S. Okyay, I. Ahmad, S. J. Kim, N. Park, H. Y. Jeong, J. B. Baek, *Nat. Nanotechnol.* **2017**, *12*, 441; b) X. Yang, J. Sun, M. Kitta, H. Pang, Q. Xu, *Nat. Catal.* **2018**, *1*, 214; c) Z. Liang, D. Yang, P. Tang, C. Zhang, J. Biendicho, Y. Zhang, J. Llorca, X. Wang, J. Li, M. Heggen, J. David, R. Dunin-Borkowski, Y.-t. Zhou, J. Morante, A. Cabot, J. Arbiol, *Adv. Energy Mater.* **2020**, *11*, 2003507.

[14] a) M. Borghei, J. Lehtonen, L. Liu, O. J. Rojas, *Adv. Mater.* **2018**, *30*, 1703691; b) S. A. Akhade, N. Singh, O. Y. Gutierrez, J. Lopez-Ruiz, H. Wang, J. D. Holladay, Y. Liu, A. Karkamkar, R. S. Weber, A. B. Padmaperuma, M. S. Lee, G. A. Whyatt, M. Elliott, J. E. Holladay, J. L. Male, J. A. Lercher, R. Rousseau, V. A. Glezakou, *Chem. Rev.* **2020**, *120*, 11370.

[15] J. Niu, R. Shao, M. Y. Liu, Y. X. Zan, M. L. Dou, J. J. Liu, Z. P. Zhang, Y. Q. Huang, F. Wang, *Adv. Funct. Mater.* **2019**, *29*, 1905095.

[16] B. Zhou, M. Zhang, W. He, H. Wang, M. Jian, Y. Zhang, *Carbon* **2019**, *150*, 21.

[17] A. Kumar, D. K. Chaudhary, S. Parvin, S. Bhattacharyya, *J. Mater. Chem. A* **2018**, *6*, 18948.

[18] T. Q. Zhang, J. Liu, L. B. Huang, X. D. Zhang, Y. G. Sun, X. C. Liu, D. S. Bin, X. Chen, A. M. Cao, J. S. Hu, L. J. Wan, *J. Am. Chem. Soc.* **2017**, *139*, 11248.

[19] V. C. Hoang, V. Gomes, K. N. Dinh, *Electrochim. Acta* **2019**, *314*, 49.

[20] Q. Kang, M. Li, Z. Wang, Q. Lu, F. Gao, *Nanoscale* **2020**, *12*, 5159.

[21] a) Y. C. Tu, P. J. Ren, D. H. Deng, X. H. Bao, *Nano Energy* **2018**, *52*, 494; b) Y. C. Tu, J. Deng, C. Ma, L. Yu, X. H. Bao, D. H. Deng, *Nano Energy* **2020**, *72*, 104700.

[22] a) M. Shao, R. Zhang, Z. Li, M. Wei, D. G. Evans, X. Duan, *ChemComm* **2015**, *51*, 15880; b) T.-J. Wang, X. Liu, Y. Li, F. Li, Z. Deng, Y. Chen, *Nano Res.* **2019**, *13*, 79.

[23] a) X. Liu, D. D. Mishra, Y. Li, L. Gao, H. Peng, L. Zhang, C. Hu, *ACS Sustainable Chem. Eng.* **2021**, *9*, 4571; b) P. Feng, J. Li, H. Wang, Z. Xu, *ACS Omega* **2020**, *5*, 24064; c) P. Makkar, A. Malik, N. N. Ghosh, *ACS Appl. Energy Mater.* **2021**, *4*, 6015.

[24] a) J. Zhang, S. Ali, F. Liu, A. Ali, K. Wang, X. Wang, *J. Electron. Mater.* **2019**, *48*, 4196; b) X. Ma, G. Ning, C. Qi, C. Xu, J. Gao, *ACS Appl. Mater. Interfaces* **2014**, *6*, 14415.

[25] M. Patel, F. Luo, M. Khoshi, E. Rabie, Q. Zhang, C. Flach, R. Mendelsohn, E. Garfunkel, M. Szostak, H. He, *ACS Nano* **2016**, *10*, 2305.

[26] a) H. Guo, Q. C. Feng, J. X. Zhu, J. S. Xu, Q. Q. Li, S. L. Liu, K. W. Xu, C. Zhang, T. X. Liu, *J. Mater. Chem. A* **2019**, *7*, 3664; b) C. Guan, A. Sumboja, H. J. Wu, W. N. Ren, X. M. Liu, H. Zhang, Z. L. Liu, C. W. Cheng, S. J. Pennycook, J. Wang, *Adv. Mater.* **2017**, *29*, 1704117.

[27] L. Lin, L. Fu, K. Zhang, J. Chen, W. Zhang, S. Tang, Y. Du, N. Tang, *ACS Appl. Mater. Interfaces* **2019**, *11*, 39062.

[28] X. B. Zhou, X. B. Liao, X. L. Pan, M. Y. Yan, L. He, P. J. Wu, Y. Zhao, W. Luo, L. Q. Mai, *Nano Energy* **2021**, *83*, 105748.

[29] a) J. Z. Liu, L. Guo, *Matter* **2021**, *4*, 2850; b) H. L. Jiang, Q. He, Y. K. Zhang, L. Song, *Acc. Chem. Res.* **2018**, *51*, 2968.

[30] X. Bo, Y. B. Li, X. J. Chen, C. Zhao, *Chem. Mater.* **2020**, *32*, 4303.

[31] Y. Wang, H. Arandiyan, X. Chen, T. Zhao, X. Bo, Z. Su, C. Zhao, *J. Phys. Chem. C* **2020**, *124*, 9971.

[32] a) S. R. Shieh, T. S. Duffy, *Phys. Rev. B* **2002**, *66*, 134301; b) H. D. Lutz, H. Mller, M. Schmidt, *J. Mol. Struct.* **1994**, *328*, 121.

[33] a) A. Bergmann, E. Martinez-Moreno, D. Teschner, P. Chernev, M. Gliech, J. F. de Araujo, T. Reier, H. Dau, P. Strasser, *Nat. Commun.* **2015**, *6*, 8625; b) P. Gao, Y. Zeng, P. Tang, Z. X. Wang, J. F. Yang, A. P. Hu, J. L. Liu, *Adv. Funct. Mater.* **2021**, *32*, 2108644.

[34] a) C. F. Li, J. W. Zhao, L. J. Xie, J. Q. Wu, Q. Ren, Y. Wang, G. R. Li, *Angew. Chem., Int. Ed.* **2021**, *60*, 18129; b) L. L. Cao, Q. Q. Luo, J. J. Chen, L. Wang, Y. Lin, H. J. Wang, X. K. Liu, X. Y. Shen, W. Zhang, W. Liu, Z. M. Qi, J. Jiang, J. L. Yang, T. Yao, *Nat. Commun.* **2019**, *10*, 4849.

[35] a) K. Fan, H. Y. Zou, Y. Lu, H. Chen, F. S. Li, J. X. Liu, L. C. Sun, L. P. Tong, M. F. Toney, M. L. Sui, J. G. Yu, *ACS Nano* **2018**, *12*, 12369; b) F. Hu, M. Patel, F. X. Luo, C. Flach, R. Mendelsohn, E. Garfunkel, H. X. He, M. Szostak, *J. Am. Chem. Soc.* **2015**, *137*, 14473.

[36] M. R. Liu, Q. L. Hong, Q. H. Li, Y. H. Du, H. X. Zhang, S. M. Chen, T. H. Zhou, J. Zhang, *Adv. Funct. Mater.* **2018**, *28*, 1801136.

[37] S. Sun, Y. Sun, Y. Zhou, S. Xi, X. Ren, B. Huang, H. Liao, L. P. Wang, Y. Du, Z. Xu, *Angew. Chem., Int. Ed.* **2019**, *58*, 6042.

[38] a) Z. Xiao, Y. Wang, Y.-c. Huang, Z. Wei, C. Dong, J. Ma, S. Shen, Y. Li, S. Wang, *Energy Environ. Sci.* **2017**, *10*, 2563; b) S. Pan, X. Mao, J. Yu, L. Hao, A. Du, B. Li, *Inorg. Chem. Front.* **2020**, *7*, 3327; c) H. Zeng, M. Oubla, X. Zhong, N. Alonso-Vante, F. Du, Y. Xie, Y. Huang, J. Ma, *Appl. Catal. B* **2021**, *281*, 119535.